



Minerva Access is the Institutional Repository of The University of Melbourne

Author/s:

Liu, C;Suvorova, S;Evans, RJ;Moran, B;Melatos, A

Title:

Bayesian Detection of a Sinusoidal Signal With Randomly Varying Frequency

Date:

2022-01-01

Citation:

Liu, C., Suvorova, S., Evans, R. J., Moran, B. & Melatos, A. (2022). Bayesian Detection of a Sinusoidal Signal With Randomly Varying Frequency. *IEEE Open Journal of Signal Processing*, 3, pp.246-260. <https://doi.org/10.1109/OJSP.2022.3186850>.

Persistent Link:

<https://hdl.handle.net/11343/318307>

License:

[CC BY](#)

Bayesian Detection of a Sinusoidal Signal with Randomly Varying Frequency

Changrong Liu, S. Suvorova, R. J. Evans, *Life Fellow, IEEE*, B. Moran, *Member, IEEE*, A. Melatos

The problem of detecting a sinusoidal signal with randomly varying frequency has a long history. It is one of the core problems in signal processing, arising in many applications including, for example, underwater acoustic frequency line tracking, demodulation of FM radio communications, laser phase drift in optical communications and, recently, continuous gravitational wave astronomy. In this paper we describe a Markov Chain Monte Carlo based procedure to compute a specific detection posterior density. We demonstrate via simulation that our approach results in an up to 25 percent higher detection rate than Hidden Markov Model based solutions, which are generally considered to be the leading techniques for these problems.

Index Terms—Bayesian detector, Hidden Markov Model, Markov Chain Monte Carlo, posterior distribution, randomly varying frequency

I. INTRODUCTION

The problem of detecting a sinusoidal signal with randomly varying frequency, measured in additive noise, is encountered in numerous applications. Our interest derives from attempts to detect the presence of as yet undiscovered gravitational waves hypothesized to emanate from rotating astronomical objects like neutron stars [1], [2], whose frequency wanders slowly and randomly [3]. Attempts to develop optimal and good sub-optimal solutions have occupied many signal processing researchers for at least 50 years, including more recent work in [4]–[7]. In essence, the problem can be categorized as detection of a non-Gaussian random process in Gaussian noise, and the forms of the optimal detector are well known [8], [9]. However, these require the conditional-mean estimate of the signal which, apart for a small number of cases, is extremely difficult to characterize and compute.

Many approximate solutions have been developed including use of an extended Kalman filter (EKF) to track the random frequency followed by a coherent detector [10], [11]. This approach is known to be far from optimal because of the simple linearization used in the EKF. Another commonly used approximation is to assume a quadratic detector structure [12] and optimize a relevant performance cost, typically

the deflection ratio. This approach leads to the use of the covariance of the random signal in the quadratic detector, but this is not optimal for a non-Gaussian random signal. One class of approximate methods relies on Hidden Markov Models (HMMs) and the Viterbi algorithm [13]–[15] to rapidly compute the maximum a posteriori (MAP) estimate using the short-time discrete Fourier transform (DFT). The detector is then formed by substituting in the MAP estimate. These methods rely on a Markov assumption for the wandering frequency dynamics between time blocks. An extension of this method enforces phase continuity between time blocks [16], resulting in a further improvement. Attempts to replace the short-time DFT with more sophisticated time-frequency analysis methods, such as the Wigner-Ville distribution, appear to offer no performance advantage over a standard Viterbi approach in terms of frequency tracking accuracy or detection performance [17].

In this paper we form the detection statistic by directly computing a specified posterior density using Markov Chain Monte Carlo (MCMC) [18] methods. The essential idea behind MCMC is to construct a Markov chain of which the invariant distribution is the desired posterior distribution. When the Markov chain converges to its equilibrium, the samples generated by the chain are essentially samples from the posterior distribution of interest [18]. To construct the detector, we introduce a time-invariant binary random variable k that indicates whether a signal is present in the data or not. Thus, under the null hypothesis H_0 , ($k = 0$), the signal of interest is absent and under the alternative hypothesis H_1 , ($k = 1$), the signal is present, with unknown amplitude and wandering frequency. The detection statistic is then set to be the posterior distribution of k , given observations \mathbf{y} , denoted by $\Pr(k|\mathbf{y})$. This posterior involves two distinct terms, $\Pr(k = 0|\mathbf{y})$ and $\int_{\Theta} \Pr(k = 1, \theta|\mathbf{y})d\theta$, with θ being a parameter in the space Θ of unknown amplitude, wandering frequency and phase of the signal under $k = 1$. We show, in order to evaluate $\Pr(k|\mathbf{y})$, we have to estimate θ as well. A closely related idea is used in [19], where the signal is modelled as a superposition of several single frequency sinusoids; in that case the number of sinusoids as well as their corresponding (constant) frequencies is estimated. We differ from previous work in that we focus on

The authors acknowledge support from the Australian Research Council (ARC) through the Centre of Excellence for Gravitational Wave Discovery (OzGrav) (grant number CE170100004) and an ARC Discovery Project (grant number DP170103625).

Changrong Liu is with the Department of Electrical and Electronic Engineering, University of Melbourne, Parkville, Victoria 3010, Australia (e-mail: changrongl1@student.unimelb.edu.au).

S. Suvorova is with the Department of Electrical and Electronic Engineering, University of Melbourne, Parkville, Victoria 3010, Australia and Australian Research Council Centre of Excellence for Gravitational Wave Discovery (OzGrav) (e-mail: sofia.suvorova@unimelb.edu.au).

R. J. Evans is with the Department of Electrical and Electronic Engineering, University of Melbourne, Parkville, Victoria 3010, Australia and Australian Research Council Centre of Excellence for Gravitational Wave Discovery (OzGrav) (e-mail: robinje@unimelb.edu.au).

B. Moran is with the Department of Electrical and Electronic Engineering, University of Melbourne, Parkville, Victoria 3010 (e-mail: wmoran@unimelb.edu.au).

A. Melatos is with the School of Physics, University of Melbourne, Parkville, Victoria 3010, Australia and Australian Research Council Centre of Excellence for Gravitational Wave Discovery (OzGrav) (e-mail: amelatos@unimelb.edu.au).

detecting one wandering frequency line, modelled as a high dimensional unknown parameter vector. The generalization to multiple signals is straightforward, albeit at the price of increased computational complexity.

In this work we follow an important extension to the basic MCMC method, called *reversible jump MCMC* (RJCMC) [20], which allows samples to jump between multiple spaces with different dimensions while maintaining overall equilibrium. We first derive the posterior distribution $\Pr(k|\mathbf{y})$ and proceed to build it with RJCMC. We then introduce a new method for efficiently proposing a candidate frequency path while maintaining a reasonable acceptance ratio. We develop a parametrized model of frequency dynamics with varying parameter dimension, where we track the frequency at coarsely spaced time samples (“knots”) while interpolating between knots with quadratic polynomials. The time between two adjacent knots is referred to here as a “block”. The number of knots in this scheme is equal to the number of blocks. We show significant saving of computational resources with a reduced numbers of knots, sufficient to capture the dynamics of the underlying frequency. This characteristic is valuable since real life applications usually deal with very large amounts of data (e.g. observation data of gravitational waves typically involves a scalar amplitude channel sampled $\sim 10^{11}$ times over an observation period lasting one year [2]). We also illustrate how to choose the number of blocks for HMM and MCMC respectively. In the end, we perform numerical simulations that demonstrate higher estimation accuracy and detection probability of MCMC, compared with HMM based methods.

The remainder of this paper is organized as follows. In Section II, a parameterized signal model is presented. In Section III, the HMM-based method is briefly explained. In Section IV, the posterior distribution for detection is formally derived. The complete RJCMC procedure is developed and described in Section V, followed by novel methods of generating a new sample path and producing a proposal sample path for a single MCMC birth and update step, detailed in Algorithms 1–7. Numerical results are described in Section VI, where the detection performance of the algorithm is quantified by receiver operating characteristic (ROC) curves. The extra information provided by estimating frequency paths is presented as part of the detection algorithm, with root mean square error (RMSE) recorded. The MCMC and the HMM methods are compared in terms of these performance measures.

II. PROBLEM STATEMENT

Without loss of generality, we assume the observed real signals with real additive noise are first converted into complex signals via the Hilbert transform. Throughout this paper, all derivations and simulations are based on complex data. Let $\mathbf{y} = \{y(t_n)\}_{n=1,\dots,N}$ be the complex-valued data sequence, observed at N equally spaced instants, $t_1 \leq \dots \leq t_N$, with $t_1 = 0$ and $T \triangleq t_n - t_{n-1}$ for all n . Let $k \in \{0, 1\}$ be a statistic constant during the whole observation period, taking values 0 or 1, denoting whether the data is composed of pure noise ($k = 0$) or signal plus noise ($k = 1$). Observations \mathbf{y} ,

which can have been generated either under hypothesis H_0 or hypothesis H_1 , are given by

$$H_0 : y(t_n) = z(t_n), \quad \text{for } k = 0, \quad (1a)$$

$$H_1 : y(t_n) = a \exp(2\pi j \phi(t_n) + \psi_0) + z(t_n) \quad (1b)$$

$$= \tilde{a} \exp(2\pi j \phi(t_n)) + z(t_n), \quad \text{for } k = 1, \quad (1c)$$

for $n = 1, 2, \dots, N$, where ψ_0 in (1b) is the unknown initial phase and, for simplicity, we incorporate it into \tilde{a} in (1c) where $\tilde{a} \triangleq a \exp(j\psi_0)$ indicates the unknown complex-valued random amplitude. This allows us to assume that the phase path starts from $\phi(t_1) = 0$. In our context, \tilde{a} and ψ_0 are treated as nuisance parameters. The noise, $z(t_n) \sim \mathcal{CN}(0, \sigma^2)$ is distributed as a complex Gaussian with variance σ^2 . The unknown signal $\mathbf{y}_c = \{y_c(t_n)\}_{n=1,\dots,N}$ is modelled by

$$y_c(t_n) = \tilde{a} \exp(2\pi j \phi(t_n)), \quad n = 1 \dots N. \quad (2)$$

Assuming that the continuous time-varying frequency is a Wiener process with zero drift and diffusion constant γ , we have

$$\begin{cases} \phi(t) = \int_0^t f(s) ds \\ df(t) = \gamma dB(t) \end{cases}, \quad (3)$$

where $B(t)$ is the standard Wiener process with $E[B(s)B(t)] = \min(s, t)$. Then the discretized counterpart with sampling interval T is

$$\begin{cases} \phi(t_{n+1}) = \phi(t_n) + f(t_n)T + w_1(t_n) \\ f(t_{n+1}) = f(t_n) + w_2(t_n) \end{cases}, \quad (4)$$

for $n = 1, 2, \dots, N - 1$, with $w_1(t_n)$ and $w_2(t_n)$ representing the instantaneous phase and frequency noise, which are both zero mean Gaussian random variables.

Introduction of the state variable $\mathbf{x}(t_n) = [\phi(t_n), f(t_n)]^T$, allows us to write (4) in matrix form as

$$\mathbf{x}(t_{n+1}) = \begin{bmatrix} 1 & T \\ 0 & 1 \end{bmatrix} \mathbf{x}(t_n) + \mathbf{w}(t_n); \quad n = 1, 2, \dots, N - 1. \quad (5)$$

The covariance matrix of $\mathbf{w}(t_n) = [w_1(t_n) \ w_2(t_n)]^T$ is assumed to be time invariant and can be represented as [16]

$$E[\mathbf{w}\mathbf{w}^T] = \begin{bmatrix} T^3/3 & T^2/2 \\ T^2/2 & T \end{bmatrix} \gamma^2. \quad (6)$$

The derivation of (6) is given in Appendix A.

For the rest of the paper the state path is denoted by $\mathbf{x} = \{\mathbf{x}(t_n)\}_{n=1,\dots,N}$, the frequency path by $\mathbf{f} = \{f(t_n)\}_{n=1,\dots,N}$, and the phase path by $\phi = \{\phi(t_n)\}_{n=1,\dots,N}$. Given observations \mathbf{y} , our decision of either H_0 or H_1 is based on the posterior distribution $\Pr(k|\mathbf{y})$.

III. HIDDEN MARKOV MODEL (HMM)

Before deriving $\Pr(k|\mathbf{y})$, we give a brief review of the widely accepted HMM-based Viterbi algorithm. In this method, the hidden state variable is the frequency, discretized into frequency bins, while the observations are divided into time blocks. The state dynamics capture the frequency wandering between the blocks into the transition probability matrix. A good choice for the transition probability in this context is

$$\Pr(F_k|F_{k-1}) = 1/3, \quad |F_k - F_{k-1}| \leq \text{frequency bin width}, \quad (7)$$

and zero elsewhere. Here F_k and F_{k-1} denote the bin-discretized frequencies at neighbouring time blocks. The emission probability matrix is constructed by computing the absolute value of the DFTs for each time block. The method relies on the assumption that the frequency is contained in one frequency bin within each block and jumps only occur between blocks. Hence, the size of the block is determined by the dynamics of the underlying wandering frequency, as explained in Section VI-D1. The hidden states are then estimated using the Viterbi algorithm and the detection statistics are determined by the "Viterbi score". A detailed analysis can be found in [16]. Unlike the HMM-based technique, where detection follows the estimation of the hidden frequency path, in our approach we form the detection statistic directly by computing $\Pr(k|\mathbf{y})$ using Bayes formula. This analysis is done in the next section.

IV. DETECTION STATISTICS BASED ON POSTERIOR DISTRIBUTION

In this section, we derive the expression of the posterior distribution $\Pr(k|\mathbf{y})$ of the detection statistic. In order to evaluate $\Pr(k|\mathbf{y})$, the term $\Pr(\tilde{a}, \mathbf{x}, k = 1|\mathbf{y})$ has to be computed, which provides us additional information about parameters other than k . In other words, the two distinct objectives, estimation and detection, normally done sequentially (as in the HMM described in Section III), are integrated naturally into one single term through this posterior distribution.

A. Structure of the detection statistic $\Pr(k|\mathbf{y})$

Using the law of total probability and Bayes' Rule, we write

$$\Pr(k = 0|\mathbf{y}) \propto \Pr(\mathbf{y}|k = 0) \Pr(k = 0) \quad (8a)$$

$$\Pr(k = 1|\mathbf{y}) = \int_D \int_{\mathbb{C}} \Pr(\tilde{a}, \mathbf{x}, k = 1|\mathbf{y}) d\tilde{a} d\mathbf{x}, \quad (8b)$$

where \mathbb{C} denotes the complex numbers and D denotes the domain for \mathbf{x} . Marginalizing out the parameters in (8b) is nontrivial since \mathbf{x} is high dimensional. Hence, we have to evaluate the integrand $\Pr(\tilde{a}, \mathbf{x}, k = 1|\mathbf{y})$ by computing the posterior estimate for the parameters in H_1 space.

B. Prior distributions

For later use, we specify the prior distributions for all parameters used in the algorithm. The prior for k is assumed to be Bernoulli distributed with a tunable parameter $1 - \alpha$, that of \tilde{a} under $k = 1$, i.e., when the signal exists, is chosen to be a complex Gaussian distribution, with mean 0 and variance Δ , i.e., $\tilde{a} \sim \mathcal{CN}(0, \Delta)$. Usually we set Δ to be a large number compared to σ^2 to reflect our initial uncertainty. As stated earlier $\phi(t_1) = 0$ and $f(t_1)$ is chosen to be uniformly distributed on the frequency interval $(0, U)$, i.e., $U \sim \mathcal{U}(0, U)$ with $0 < U \leq 1/T$, where U denotes the bandwidth of \mathbf{y}_c and $1/T$ is the sampling rate. The bandwidth is either known,

or, as here, assumed to be equal to the Nyquist frequency, so that $U = 1/T$, although this is not very critical.¹

C. Main result

The main result of this work is the following theorem.

Theorem IV.1. *The posterior for k is*

$$\Pr(k = 0|\mathbf{y}) \propto \alpha W_0 \quad (9a)$$

$$\Pr(k = 1|\mathbf{y}) \propto (1 - \alpha) W_0 \int_D \int_{\mathbb{C}} W_f W_{\tilde{a}} d\tilde{a} d\mathbf{x} \quad (9b)$$

$$\Pr(\tilde{a}, \mathbf{x}, k = 1|\mathbf{y}) \propto (1 - \alpha) W_0 W_f W_{\tilde{a}}, \quad (9c)$$

with

$$W_0 = \frac{1}{(\pi\sigma^2)^N} \exp\left(-\frac{1}{\sigma^2} \mathbf{y}^H \mathbf{y}\right), \quad (10)$$

where the superscript H denotes conjugate transpose,

$$W_f = \left(\frac{q\sigma^2}{U\Delta}\right) \exp[\eta(\mathbf{x})], \quad f(t_1) \in (0, U), \quad (11)$$

and

$$W_{\tilde{a}} = \frac{1}{\pi\sigma^2 q} \exp\left[-\frac{1}{\sigma^2 q} |\tilde{a} - \bar{a}|^2\right], \quad (12)$$

where

$$q = (N + \sigma^2/\Delta)^{-1} \quad (13a)$$

$$\bar{a} = q \mathbf{D}_f^H \mathbf{y} \quad (13b)$$

$$\mathbf{D}_f = \exp(j2\pi\phi) \quad (13c)$$

$$\eta(\mathbf{x}) = \frac{q}{\sigma^2} (\mathbf{D}_f^H \mathbf{y})^H (\mathbf{D}_f^H \mathbf{y}) = \frac{|\bar{a}|^2}{\sigma^2 q}. \quad (13d)$$

Proof. The likelihood W_0 is

$$W_0 \triangleq \Pr(\mathbf{y}|k = 0) = \frac{1}{(\pi\sigma^2)^N} \exp\left(-\frac{1}{\sigma^2} \mathbf{y}^H \mathbf{y}\right). \quad (14)$$

As we show later, our algorithm does not require numerical computation of W_0 because it cancels out.

We have

$$\Pr(\tilde{a}, \mathbf{x}, k = 1|\mathbf{y}) \propto \Pr(\tilde{a}, \mathbf{x}, k = 1) \Pr(\mathbf{y}|\tilde{a}, \mathbf{x}, k = 1), \quad (15)$$

where the likelihood term $\Pr(\mathbf{y}|\tilde{a}, \mathbf{x}, k = 1)$ is rewritten as

$$\frac{1}{(\pi\sigma^2)^N} \exp\left[-\frac{1}{\sigma^2} (\mathbf{y} - \tilde{a} \mathbf{D}_f)^H (\mathbf{y} - \tilde{a} \mathbf{D}_f)\right], \quad (16)$$

with

$$\mathbf{D}_f = \exp(j2\pi\phi). \quad (17)$$

The other factor $\Pr(\tilde{a}, \mathbf{x}, k = 1)$ is further expanded to

$$\Pr(\tilde{a}, \mathbf{x}, k = 1) = \Pr(k = 1) \Pr(\tilde{a}, \mathbf{x}|k = 1), \quad (18)$$

where $\Pr(\tilde{a}, \mathbf{x}|k = 1)$ denotes the prior distribution for \tilde{a} and \mathbf{x} under the model $k = 1$. As for the prior distribution of \mathbf{x} , given an initial state of the path $\mathbf{x}(t_1)$, the statistical representation of the whole state path \mathbf{x} is determined by the model according

¹In gravitational wave applications, U is usually much smaller than the sampling rate. A typical continuous wave search is conducted over sub-bands of ~ 1 Hz to facilitate handling the large volume of data involved, compared to the sampling frequency $\gtrsim 1$ kHz. Continuous wave signals from neutron stars are expected to be quasimonochromatic, with intrinsic frequency bin width $\lesssim 10^{-6}$ Hz [2].

to (5). Based on the above analysis and the prior distributions, we rewrite (15) as

$$\begin{aligned} \Pr(\tilde{a}, \mathbf{x}, k = 1 | \mathbf{y}) &\propto \frac{1 - \alpha}{U\pi\Delta(\pi\sigma^2)^N} \exp(-\tilde{a}^H \tilde{a} / \Delta) \\ &\times \exp\left[-\frac{1}{\sigma^2}(\mathbf{y} - \tilde{a}\mathbf{D}_f)^H(\mathbf{y} - \tilde{a}\mathbf{D}_f)\right]. \end{aligned} \quad (19)$$

To assist MCMC sampling we now expand the quadratic form in (19) and after some algebraic manipulations, rewrite it in the following way

$$\begin{aligned} &\exp\left[-\frac{1}{\sigma^2}(\mathbf{y} - \tilde{a}\mathbf{D}_f)^H(\mathbf{y} - \tilde{a}\mathbf{D}_f)\right] \exp(-\tilde{a}^H \tilde{a} / \Delta) \\ &= \exp\left[-\frac{1}{\sigma^2 q}(\tilde{a} - \bar{a})^H(\tilde{a} - \bar{a})\right] \exp\left(-\frac{1}{\sigma^2} \mathbf{y}^H \mathbf{y}\right) \quad (20) \\ &\times \exp\left[\frac{q}{\sigma^2}(\mathbf{D}_f^H \mathbf{y})^H(\mathbf{D}_f^H \mathbf{y})\right], \end{aligned}$$

with

$$q = (\mathbf{D}_f^H \mathbf{D}_f + \sigma^2 / \Delta)^{-1} = (N + \sigma^2 / \Delta)^{-1} \quad (21a)$$

$$\bar{a} = q \mathbf{D}_f^H \mathbf{y}. \quad (21b)$$

Notice that \bar{a} is simply the least squares solution of \tilde{a} in (1c) for a given \mathbf{D}_f . We now define

$$W_{\tilde{a}} \triangleq \Pr(\tilde{a} | \mathbf{D}_f, \mathbf{y}, k = 1) = \frac{1}{\pi\sigma^2 q} \exp\left[-\frac{1}{\sigma^2 q} |\tilde{a} - \bar{a}|^2\right] \quad (22)$$

as the normal distribution of \tilde{a} given a specific draw \mathbf{D}_f , with mean \bar{a} and variance $\sigma^2 q$. Equation (12) reflects our uncertainty of \tilde{a} relative to \bar{a} in consequence of the observation noise. Combining the remaining terms of (19) and (20), we obtain

$$\begin{aligned} W_f &\triangleq \frac{q\sigma^2}{U\Delta} \exp\left[\frac{q}{\sigma^2}(\mathbf{D}_f^H \mathbf{y})^H(\mathbf{D}_f^H \mathbf{y})\right] \\ &= \frac{q\sigma^2}{U\Delta} \exp\left(\frac{|\bar{a}|^2}{\sigma^2 q}\right) \quad (23) \\ &= \frac{q\sigma^2}{U\Delta} \exp\eta(\mathbf{x}). \end{aligned}$$

Specifically, $\eta(\mathbf{x})$ can be interpreted as the signal-to-noise ratio (SNR) evaluated along a sampled state path \mathbf{x} . Combining (19) (22) and (23), we obtain the formulae for $\Pr(k = 0 | \mathbf{y})$ and $\Pr(k = 1 | \mathbf{y})$ as given in (9b) (9c). \square

Corollary IV.1.1. *The posterior distribution for k is approximated by*

$$\Pr(k | \mathbf{y}) = \begin{cases} \frac{\alpha}{\alpha + (1-\alpha)W}, & k = 0 \\ \frac{(1-\alpha)W}{\alpha + (1-\alpha)W}, & k = 1 \end{cases} \quad (24)$$

with

$$W \approx \left(\frac{\sigma^2}{N\Delta}\right)^{1/2} \exp\left[\max_{\mathbf{x}}[\eta(\mathbf{x})]\right]. \quad (25)$$

Proof. To further evaluate the integral term defined in (9b), we define

$$W \triangleq \int_{\mathcal{C}} W_{\tilde{a}} d\tilde{a} \int_{\mathcal{D}} W_f d\mathbf{x} \quad (26a)$$

$$\approx \left(\frac{\sigma^2}{N\Delta}\right)^{1/2} \exp\left[\max_{\mathbf{x}}[\eta(\mathbf{x})]\right]. \quad (26b)$$

The first integral in (26a) is equal to unity. Evaluation of the second integral uses the Laplace approximation, based on the assumption that the integrand is strongly and singly peaked. The expression $\max_{\mathbf{x}}[\eta(\mathbf{x})]$ in (26b) is easy to evaluate for constant frequency signals through the Fourier transform $\mathcal{F}(\mathbf{y})$, i.e.,

$$\eta(\mathbf{x}) = |\mathcal{F}(\mathbf{y})|^2 / \sigma^2, \quad (27)$$

but to compute (26a) for a wandering path, we resort to the MCMC algorithm in V. \square

V. MCMC ALGORITHM

A. Basic principle

Formally, the posterior probability of a parameter μ , given data D is given by

$$\Pr(\mu | D) = \frac{\Pr(D | \mu) \Pr(\mu)}{\int_{\mu \in \mathbb{S}} \Pr(D | \mu) \Pr(\mu) d\mu} \quad (28)$$

where \mathbb{S} is the domain of the parameters and $\Pr(\mu)$ and $\Pr(D | \mu)$ are the prior probability and likelihood probability, respectively. Equation (28) is often hard to compute analytically because of the potentially high dimensional integration appearing in the denominator.

MCMC provides a way to compute (28) without evaluating the denominator by the construction of a Markov chain with equilibrium distribution as in (28). After MCMC converges, samples drawn from the Markov chain can be treated as random samples drawn from the true posterior distribution. The Maximum a Posteriori (MAP) estimate or other statistical quantities can then be approximated using these ensemble samples.

Specific algorithms designed for our scenario are described in detail in the following sections.

B. Sampling rules

In this section, based on (9), we construct the specific MCMC algorithm for computing $\Pr(k | \mathbf{y})$. We use $(\cdot)^i$ to denote the value at the i th iteration and $(\cdot)'$ to denote the proposed value. Firstly, we specify a recipe for proposals to either switch between different hypotheses (“birth”/“death”) or explore parameter space (“update”) under hypothesis H_1 (or $k = 1$). That is, we build a finite state machine (Fig. (1)) of which the output returns the instruction for the next move. Specifically, we introduce a new random Boolean variable s^i . It evolves as a Markov chain with a given transition matrix Γ , as defined in Table (IV). The value of s^i combined with the previous k value k^{i-1} gives the instruction to either jump between H_0 and H_1 or search within H_1 . Algorithms 2-7 in Appendix B describe the implementation of MCMC as well as “birth”, “death” and “update” in more detail. From (9), the

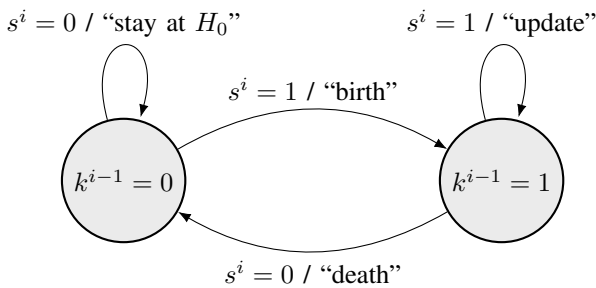


Fig. 1. Diagram of the finite state machine to generate MCMC proposals

acceptance ratio for traversing between “birth”, “death” and “update” proposals at the i th iteration are, respectively,

$$r_{\text{birth}} \triangleq \frac{(1 - \alpha)W'_f W'_a}{\alpha} \quad (29a)$$

$$r_{\text{death}} \triangleq \frac{\alpha}{(1 - \alpha)W_f^{i-1} W_a^{i-1}} \quad (29b)$$

$$r_{\text{update}} \triangleq \frac{W'_f W'_a}{W_f^{i-1} W_a^{i-1}}, \quad (29c)$$

where W'_f and W'_a are evaluated at the proposed (perhaps rejected) sample values \mathbf{x}' and \tilde{a}' at the current iteration, according to (11) and (12), and W_f^{i-1} and W_a^{i-1} are obtained from previous values \mathbf{x}^{i-1} and \tilde{a}^{i-1} . The acceptance probabilities are then

$$A_{\text{birth}} \triangleq \min(1, r_{\text{birth}}) \quad (30a)$$

$$A_{\text{death}} \triangleq \min(1, r_{\text{death}}) \quad (30b)$$

$$A_{\text{update}} \triangleq \min(1, r_{\text{update}}). \quad (30c)$$

C. Knot-interpolation Scheme to Reduce Parameter Dimension

High dimensionality of the parameter space may cause convergence problems for MCMC [21]. To alleviate this problem, for both the HMM and MCMC approaches, the time series \mathbf{y} (of length N and sampled at time intervals of length T) is partitioned into consecutive blocks of equal time duration, T_b , though the chosen lengths of these blocks will differ between the two approaches. The endpoints of these blocks, at intervals of time length T_b are called the *knots*. The number of blocks is N_b , so that $NT = N_b T_b$. As described in Section III, the HMM-based method requires calculation of the DFT of each block to produce the emission probabilities, whereas in the MCMC approach a quadratic interpolation between the knots is used to approximate the time series and reduce dimensionality, as we only sample \mathbf{x} 's at the knots. The interpolation between the knots is performed in the following way

$$\begin{cases} \tilde{\phi}(t_{Mm+1+\ell}) &= \phi(t_{Mm+1}) + f(t_{Mm+1})T\ell \\ &\quad + \frac{1}{2}b_1^m(T\ell)^2 + \frac{1}{3}b_2^m(T\ell)^3 \\ \tilde{f}(t_{Mm+1+\ell}) &= f(t_{Mm+1}) + b_1^m T\ell + b_2^m(T\ell)^2, \end{cases} \quad (31)$$

where $M = N/N_b$ and $\ell = 0, \dots, M - 1$ denote time epochs within the m th block and $T_b = MT$ is the time duration

of one block, as mentioned above. Notice that the resulting interpolated path $\{\tilde{\phi}(t_n), \tilde{f}(t_n)\}_{n=1, \dots, N}$ is of length N . The continuity of the interpolated path is ensured by solving (31) for b_1^m and b_2^m using the values at the knots.

Denoted by the function “Interp”, this procedure is described in Appendix B Algorithm 1. The dynamics between the knots is identical to the dynamics in (5) with T replaced by T_b . The rationale for choosing T_b (or equivalently, N_b) is discussed in Section VI-D2.

From now we focus on generating the sequence of values, \mathbf{x}_{N_b} , of the path at the knots, in “birth” and “update” scenarios. For simplicity of notation, we indicate the elements of \mathbf{x}_{N_b} by $\mathbf{x}_{N_b}(j)$ for $j = 1, \dots, N_b$.

D. Generating a sample path \mathbf{x}'_{N_b} (“birth”)

For the MCMC “birth” procedure, we generate a random path \mathbf{x}'_{N_b} with length N_b and individual elements

$$\mathbf{x}'_{N_b}(j+1) = \begin{bmatrix} 1 & T_b \\ 0 & 1 \end{bmatrix} \mathbf{x}'_{N_b}(j) + \mathbf{w}(j). \quad (32)$$

The noise term $\mathbf{w}(j)$ is calculated in the same way as in (6), with T replaced by T_b . Here we define

$$\mathbf{C} \triangleq E[\mathbf{w}(j)\mathbf{w}(j)^T] = \gamma^2 \begin{bmatrix} T_b^3/3 & T_b^2/2 \\ T_b^2/2 & T_b \end{bmatrix}, \quad (33)$$

for $j = 1, 2, \dots, N_b - 1$.

E. Updating a proposal path \mathbf{x}'_{N_b} from previous path $\mathbf{x}^{i-1}_{N_b}$

It is important in the MCMC algorithm to formulate a good update proposal that specifies the probability of moving to a new point in parameter space — a stochastic path \mathbf{x}'_{N_b} , given previous location $\mathbf{x}^{i-1}_{N_b}$. In this work, we developed a unique approach to this problem, to be described here. The desired new path \mathbf{x}'_{N_b} should possess the following properties:

- (i) it should obey the state dynamics model in (32).
- (ii) it should be “close” to the previous path to avoid a large chance of rejection. This is especially critical when the samples are near the peak of the posterior probability density function;
- (iii) the distance between paths should be controllable, to facilitate a flexible sampling scheme such as, for example, to be able to increase the convergence rate or to escape from local extrema.

Consequently, we want to control the Euclidean distance $\|\mathbf{x}'_{N_b} - \mathbf{x}^{i-1}_{N_b}\|$. To achieve this, we expand (32) as

$$\begin{bmatrix} \mathbf{x}'_{N_b}(1) \\ \mathbf{x}'_{N_b}(2) \\ \vdots \\ \mathbf{x}'_{N_b}(N_b) \end{bmatrix} = \begin{bmatrix} \mathbf{I}_2 & 0 & \dots & 0 \\ \mathbf{F} & \mathbf{I}_2 & \dots & 0 \\ \vdots & \vdots & \ddots & \vdots \\ \mathbf{F}^{N_b-1} & \mathbf{F}^{N_b-2} & \dots & \mathbf{I}_2 \end{bmatrix} \begin{bmatrix} \mathbf{x}'_{N_b}(1) \\ \mathbf{w}(1) \\ \vdots \\ \mathbf{w}(N_b - 1) \end{bmatrix} \quad (34)$$

with $\mathbf{w}(j) \sim \mathcal{N}(\mathbf{0}, \mathbf{C})$, $\mathbf{F} = \begin{bmatrix} 1 & T_b \\ 0 & 1 \end{bmatrix}$. To generate a new path, each $\mathbf{w}(j)$ is replaced by a new random vector $\mathbf{L}\mathbf{q}(j)$, where $\mathbf{L}\mathbf{L}^T = \mathbf{C}$ is the Cholesky decomposition,

and $\mathbf{q}(j) \sim \mathcal{N}(0, \mathbf{I}_2)$ is a bivariate normal vector with unit covariance matrix. Now (34) for the new path becomes

$$\begin{bmatrix} \mathbf{x}'_{N_b}(1) \\ \mathbf{x}'_{N_b}(2) \\ \vdots \\ \mathbf{x}'_{N_b}(N_b) \end{bmatrix} = \begin{bmatrix} \mathbf{I}_2 & 0 & \cdots & 0 \\ \mathbf{F} & \mathbf{I}_2 & \cdots & 0 \\ \vdots & \vdots & \ddots & \vdots \\ \mathbf{F}^{N_b-1} & \mathbf{F}^{N_b-2} & \cdots & \mathbf{I}_2 \end{bmatrix} \begin{bmatrix} \mathbf{L}\mathbf{L}^{-1}\mathbf{x}'_{N_b}(1) \\ \mathbf{L}\mathbf{q}(1) \\ \vdots \\ \mathbf{L}\mathbf{q}(N_b-1) \end{bmatrix} \quad (35a)$$

$$= \underbrace{\begin{bmatrix} \mathbf{L} & 0 & \cdots & 0 \\ \mathbf{F}\mathbf{L} & \mathbf{L} & \cdots & 0 \\ \vdots & \vdots & \ddots & \vdots \\ \mathbf{F}^{N_b-1}\mathbf{L} & \mathbf{F}^{N_b-2}\mathbf{L} & \cdots & \mathbf{L} \end{bmatrix}}_{\mathbf{M}_2} \begin{bmatrix} \mathbf{L}^{-1}\mathbf{x}'_{N_b}(1) \\ \mathbf{q}(1) \\ \vdots \\ \mathbf{q}(N_b-1) \end{bmatrix} \quad (35b)$$

$$= \mathbf{M}_2 \left(\begin{bmatrix} \mathbf{L}^{-1}\mathbf{x}'_{N_b}(1) \\ 0 \\ \vdots \\ 0 \end{bmatrix} + \begin{bmatrix} \mathbf{q}(0) \\ \mathbf{q}(1) \\ \vdots \\ \mathbf{q}(N_b-1) \end{bmatrix} \right) \quad (35c)$$

$$= \underbrace{\begin{bmatrix} \mathbf{I}_2 \\ \mathbf{F} \\ \vdots \\ \mathbf{F}^{N_b-1} \end{bmatrix}}_{\mathbf{M}_1} \mathbf{x}'_{N_b}(1) + \mathbf{M}_2 \begin{bmatrix} \mathbf{q}(0) \\ \mathbf{q}(1) \\ \vdots \\ \mathbf{q}(N_b-1) \end{bmatrix}, \quad (35d)$$

with $\mathbf{q}(0) = [0, 0]^T$ and $\mathbf{q}(j) \sim \mathcal{N}(\mathbf{0}, \mathbf{I}_2)$ for $j = 1, \dots, N_b - 1$. From (35d), we observe that a stochastic state path \mathbf{x}'_{N_b} depends purely on the random starting point $\mathbf{x}'_{N_b}(1)$ and the random noise sequence $\mathbf{q} = [\mathbf{q}^T(0), \dots, \mathbf{q}^T(N_b - 1)]^T$ since matrices \mathbf{M}_1 and \mathbf{M}_2 are deterministic. In our approach we keep $\mathbf{x}'_{N_b}(1) = \mathbf{x}_{N_b}^{i-1}(1)$ and only perturb the random noise sequence \mathbf{q} . Under the requirement (i) above, the mean and variance of the perturbed noise sequence need to be retained. Specifically, the steps for perturbing the noise sequence at the i th iteration are: given a previous path $\mathbf{x}_{N_b}^{i-1}$, first extract the random part: $\mathbf{q}^{i-1} = \mathbf{x}_{N_b}^{i-1} - \mathbf{M}_1 \mathbf{x}_{N_b}^{i-1}(1)$; then generate a white noise perturbation sequence $\mathbf{q}' = [\mathbf{q}'^T(0), \dots, \mathbf{q}'^T(N_b - 1)]$, with $\mathbf{q}'(0) = [0, 0]^T$ and random vector $\mathbf{q}'(j)$ with zero mean and unit covariance $\text{cov}(\mathbf{q}'(j)) = \mathbf{I}_2$ for $j = 1, \dots, N_b - 1$. The perturbation sequence \mathbf{q}' is independent of \mathbf{q}^{i-1} , that is $E[\mathbf{q}'(\mathbf{q}^{i-1})^T] = \mathbf{0}$. We introduce a parameter β and compute the new noise sequence as $\mathbf{q}^i = \mathbf{q}^{i-1} \cos \beta + \mathbf{q}' \sin \beta$. This perturbation scheme ensures that the new noise sequence has the required mean and variance, because of the identity $\cos^2 \beta + \sin^2 \beta = 1$. It is also apparent that $\cos \beta$ is the correlation coefficient between each old $\mathbf{q}^{i-1}(j)$ and new $\mathbf{q}^i(j)$ for $j = 1, \dots, N_b - 1$, thus the tunable parameter β helps control the "closeness" between the old and the new sequence, i.e., for smaller β , the correlation is greater, hence the perturbation is smaller.

This scheme has one problem related to the lower triangular shape of the matrix \mathbf{M}_2 . The noise in the new path $\mathbf{M}_2 \mathbf{q}^i$ tends to accumulate along the path, meaning that $\|\text{cov}(\mathbf{q}^i(n))\| >$

$\|\text{cov}(\mathbf{q}^i(m))\|$ for $n > m$ as the iteration number i increases. Our *ad hoc* solution to this problem is the following. Instead of setting $\mathbf{x}'_{N_b}(1) = \mathbf{x}_{N_b}^{i-1}(1)$, we start from a random position $l \in \{1, \dots, N_b\}$ and let $\mathbf{x}'_{N_b}(l) = \mathbf{x}_{N_b}^{i-1}(l)$; the sequence is then split into two, with one part propagating backward all the way to $\mathbf{x}'_{N_b}(1)$ and the other part propagating forward until $\mathbf{x}'_{N_b}(N_b)$. This is achieved by replacing matrices \mathbf{M}_1 and \mathbf{M}_2 by \mathbf{M}'_1 and \mathbf{M}'_2 as follows:

$$\begin{aligned} \mathbf{M}'_1 &= [\mathbf{F}^{-(l-1)} & \mathbf{F}^{-(l-2)} & \cdots & \mathbf{I}_2 & \mathbf{F} & \cdots & \mathbf{F}^{N_b-l}]^T \\ \mathbf{M}'_2 &= \begin{bmatrix} \mathbf{L} & \mathbf{F}^{-1}\mathbf{L} & \cdots & \mathbf{F}^{-(l-1)}\mathbf{L} & 0 & \cdots & 0 \\ 0 & \mathbf{L} & \cdots & \mathbf{F}^{-(l-2)}\mathbf{L} & 0 & \cdots & 0 \\ \vdots & \ddots & \vdots & \vdots & \vdots & \ddots & \vdots \\ 0 & \cdots & \mathbf{L} & \mathbf{F}^{-1}\mathbf{L} & 0 & \cdots & 0 \\ 0 & \cdots & 0 & \mathbf{L} & 0 & \cdots & 0 \\ 0 & \cdots & 0 & \mathbf{F}\mathbf{L} & \mathbf{L} & \cdots & 0 \\ \vdots & \ddots & \vdots & \vdots & \vdots & \ddots & \vdots \\ 0 & \cdots & 0 & \mathbf{F}^{N_b-l}\mathbf{L} & \mathbf{F}^{N_b-l-1}\mathbf{L} & \cdots & \mathbf{L} \end{bmatrix}. \end{aligned} \quad (36)$$

Notice that when $l = 1$, we recover $\mathbf{M}'_1 = \mathbf{M}_1$ and $\mathbf{M}'_2 = \mathbf{M}_2$. This still causes noise accumulation in \mathbf{x}'_{N_b} for elements away from l in both directions, but the random choice of l at each iteration mitigates the effect in the long run.

The correlation between previous and proposed paths is

$$\begin{aligned} \mathbf{x}'_{N_b} &= \mathbf{M}'_1 \mathbf{x}_{N_b}^{i-1}(l) + \mathbf{M}'_2 \mathbf{q}^{i-1}; \\ \mathbf{x}'_{N_b} &= \mathbf{M}'_1 \mathbf{x}_{N_b}^{i-1}(l) + \mathbf{M}'_2 \mathbf{q}^{i-1} \cos \beta + \mathbf{M}'_2 \mathbf{q}' \sin \beta; \\ \text{cov}(\mathbf{x}_{N_b}^{i-1}, \mathbf{x}'_{N_b}) &= E[\mathbf{M}'_2 \mathbf{q}^{i-1} (\mathbf{M}'_2 \mathbf{q}^{i-1} \cos \beta + \mathbf{M}'_2 \mathbf{q}' \sin \beta)^T] \\ &= (\mathbf{M}'_2)^2 \cos \beta E[\mathbf{q}^{i-1} (\mathbf{q}^{i-1})^T] \\ &= (\mathbf{M}'_2)^2 \cos \beta \mathbf{I}_{2 \times N_b}, \end{aligned} \quad (37)$$

where we use $E[\mathbf{q}^{i-1} (\mathbf{q}^{i-1})^T] = \mathbf{I}_{2 \times N_b}$, $E[\mathbf{q}^{i-1} \mathbf{q}'^T] = 0$ and $E(\mathbf{x}_{N_b}^{i-1}) = E(\mathbf{x}'_{N_b}) = \mathbf{M}'_1 \mathbf{x}_{N_b}^{i-1}(l)$. Equation (37) indicates how the correlation of previous and proposed paths can be tuned by β .

For completeness, the distance between neighbouring paths in the \mathcal{L}_2 norm is bounded by

$$\begin{aligned} \|\mathbf{x}_{N_b}^{i-1} - \mathbf{x}'_{N_b}\| &= \|\mathbf{M}'_2 \mathbf{q}^{i-1} (\cos \beta - 1) + \mathbf{M}'_2 \mathbf{q}' \sin \beta\| \\ &\leq \sigma_{\mathbf{M}'_2} \sqrt{2N_b} (\cos \beta + \sin \beta - 1), \end{aligned} \quad (38)$$

where $\sigma_{\mathbf{M}'_2}$ is the largest singular value of \mathbf{M}'_2 . The pseudocode of the method is provided in Appendix B, Algorithm 7.

VI. NUMERICAL VALIDATION

A. Description of synthetic data

To test our MCMC algorithm, a synthetic data sequence with length N is generated according to (1c), (5) and (6). Parameters for synthetic data are given in Table (I). The starting frequency $f(t_1)$ is chosen randomly from $(0, U)$ with $U = 1$. The true path sequence $\mathbf{x}_{\text{syn}} = \{\mathbf{x}_{\text{syn}}(t_n)\}_{n=1, \dots, N}$, with $\mathbf{x}_{\text{syn}}(t_n) = [\phi_{\text{syn}}(t_n), f_{\text{syn}}(t_n)]^T$, is randomly synthesised according to the dynamics given in (5) and (6); the complex-valued amplitude $\tilde{a} = |\tilde{a}| \exp(j\psi_0)$ is also chosen randomly

TABLE I
PARAMETERS FOR GENERATING SYNTHETIC TEST DATA

	Data length	Sampling interval	Diffusion constant of Wiener process	Signal-to-noise-ratio	standard deviation of observation noise
Symbol	N	$T = \frac{1}{U}$ (sec)	γ_{syn}^2 (Hz sec $^{-1/2}$)	SNR	σ (arbitrary units)
Value	1000	1	1×10^{-4}	{0.1, 0.15, 0.2}	$\sqrt{20}$

TABLE II
PRIOR DISTRIBUTION OF \mathbf{x}_1 , \tilde{a} , k , \mathbf{W}_j

$\Pr(\phi(t_1) = 0)$	$\Pr(f(t_1))$	$\Pr(\tilde{a})$	$\Pr(k = 0)$	$\Pr(k = 1)$	$\Pr(\mathbf{w}(j))$
1	$\mathcal{U}(0, U)$	$\mathcal{CN}(0, \Delta)$	α	$1 - \alpha$	$\mathcal{N}(\mathbf{0}, \mathbf{C})$

from the distribution $\mathcal{CN}(0, \Delta)$, with $\psi_0 \sim \mathcal{U}(0, 2\pi)$. The signal-to-noise ratio is $\text{SNR} = \frac{|\tilde{a}|}{\sigma}$. This SNR differs from the SNR along a path defined in (13d): $\eta(\mathbf{x})$.

B. Description of MCMC Parameters

Prior distributions of unknown parameters and specific values are given in Table (II) and Table (III) respectively. The number of blocks, N_b , is chosen from the set {5, 20, 200, 500, 1000} to investigate how it affects the runtime and detection performance. T_b is determined according to $T_b N_b = TN$. The parameters used in the implementation of the algorithms are given in Table (IV). The factor $\beta = 0.1$ is chosen experimentally to ensure a reasonable MCMC acceptance rate.

TABLE III
VALUES OF PRIOR DISTRIBUTION PARAMETERS

U (Hz)	Δ (arb.units)	α	\mathbf{C}
1	1×10^2	0.5	(33) with $\gamma = 10^{-4}$ (or $\gamma = 10^{-5}$) Hz sec $^{-1/2}$

TABLE IV
PARAMETERS APPEARING IN ALGORITHM 2-7

Number of iterations $N_{\text{iteration}}$	Transition matrix Γ for s^2	Correlation factor β	Diffusion constant of Wiener process γ
1×10^5	$\begin{bmatrix} 0.5 & 0.5 \\ 0.5 & 0.5 \end{bmatrix}$	0.1	$\{10^{-4}, 10^{-5}\}$

C. MCMC-posterior distributions

In Section IV and V, we show that, to compute the posterior $\Pr(k|\mathbf{y})$, we have to sample from $\Pr(k = 1, \tilde{a}, \mathbf{x}|\mathbf{y})$ as well as $\Pr(k = 0|\mathbf{y})$. Hence, as a part of the detection algorithm, we approximate the MCMC-posterior for the state path \mathbf{x}

²We differentiate γ_{syn} from γ , the first one is used in generating synthetic data, and the second one is the parameter of MCMC algorithms. The chosen value of γ_{syn} is to reflect the degree of randomness of the wandering frequency.

as well, which is achieved by simply collecting all of the sampled state paths under $k = 1$. The MCMC-MAP estimate is achieved by calculating the mode of these paths. Since the HMM algorithm also estimates \mathbf{x} , it is of interest to compare these two algorithms in terms of the estimated paths.

The MCMC-posterior for k : $\Pr(k|\mathbf{y})$ is approximated by counting the number of occurrences of $k = 1$ and $k = 0$ respectively. A Neyman-Pearson type detector is constructed by comparing $\Pr(k|\mathbf{y})$ with a pre-defined threshold to determine detection.

In the following sections, we compute the MCMC-posterior distributions for \mathbf{x} and k , respectively. Related performance criteria like estimation error and ROC curves are also presented.

D. Rationale for choosing the number of blocks (knots)

In this section we discuss the reasoning behind the differences in the selection of the number of blocks for the HMM and MCMC methods.

1) For HMM

In HMM, within one block, we perform an M -point DFT, resulting in frequency bins of width $\Delta f = U/M$, where U and M , as in MCMC, denote the bandwidth of the signal and block size, respectively. The number of blocks N_b , or equivalently, M is chosen such that

$$\Pr\left(\int_0^{T_b} df(s) \geq \Delta f\right) < \kappa, \quad (39)$$

where $T_b = TM$ is the time duration within one block and κ is restricted to be a small number. With $f(t)$ undergoing the dynamics in (3), the integral in (39) is

$$\int_0^{T_b} df(s) = \gamma(B(T_b) - B(0)) \sim \mathcal{N}(0, \gamma^2 T_b), \quad (40)$$

where $B(t)$ denotes the Wiener process at time t .

We set the frequency bin width to be twice the standard deviation in (40), i.e., $\Delta f = 2\gamma\sqrt{T_b}$. Combining the relation that $\Delta f = U/M$ and setting $\gamma = 1 \times 10^{-4}$ (Table. (I)), we finally choose $N_b = N/M = 5$ for the HMM in the following experiments.

2) For MCMC

To implement our MCMC algorithm, N_b needs to be chosen beforehand. The optimum N_b , could be computed by maximizing the likelihood ratio or deflection ratio, as in [22]. In this section we describe an alternative, intuitive reasoning behind our choice of N_b for the MCMC.

Consider the two matrices defined in (35), one of which is the full $2N \times 2N$ matrix \mathbf{M}_2 and the other is the $2N_b \times 2N_b$ matrix \mathbf{M}_2^b . By design, \mathbf{M}_2^b is constructed from \mathbf{M}_2 by keeping the rows and columns at the knots and removing the rest. The difference in ‘‘information’’ between these two matrices is captured by the difference between the information theoretic ‘‘Shannon entropy’’ $H(N)$ and $H(N_b)$ of the singular values of \mathbf{M}_2 and \mathbf{M}_2^b respectively. For any \mathbf{M}_2^b we write

$$H(N_b) = - \sum_i \xi_i^b \log(\xi_i^b), \quad (41)$$

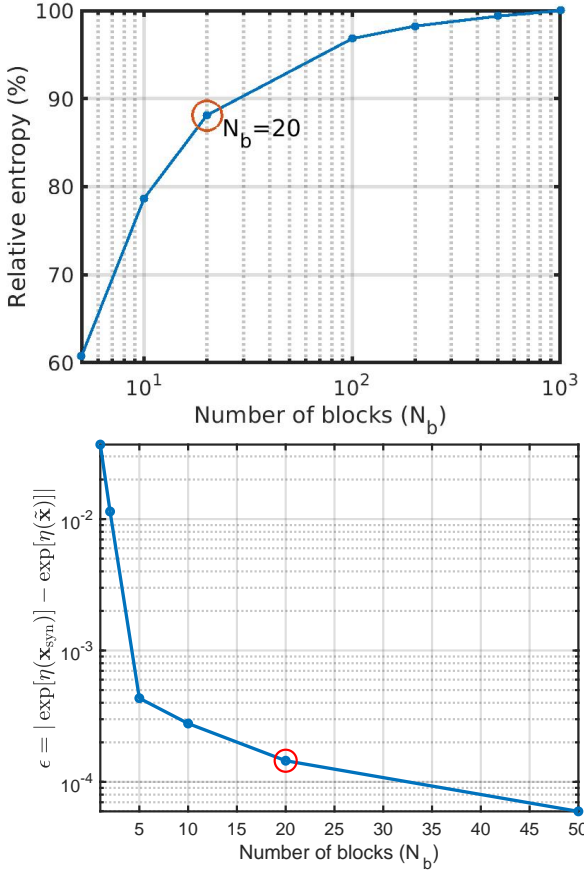


Fig. 2. Upper panel: Relative entropy between full dynamic matrix \mathbf{M}_2^H and reduced matrices \mathbf{M}_2 as a function of N_b . The entropy associated with $N_b = 20$ is circled in red, indicating 10 percent information reduction. Lower panel: Absolute value of error caused by block approximation, i.e. coarse-graining error of the state path \mathbf{x} versus block size, where the error is $\epsilon = |\exp[\eta(\mathbf{x}_{\text{syn}})] - \exp[\eta(\tilde{\mathbf{x}})]|$.

where $\xi_i^b = \sigma_i / \sum_{j=1}^{2N_b} \sigma_j^b$ and σ_j^b is the j th largest non-zero singular value of \mathbf{M}_2^b . The entropy $H(N)$ is computed for the full matrix \mathbf{M}_2 . This entropy is effectively the same as the von Neumann entropy [23] in the context of symmetric matrices. Accordingly, for a chosen set of parameters, we compute the entropy for a given N_b relative to $H(N)$ of the full matrix. The result is shown on the left hand panel in Fig. (2).

To strengthen the entropy claim, we also directly evaluate $\exp[\eta(\mathbf{x}_{\text{syn}})]$ ((13d)). This is the dominant term contributing to the Bayesian evidence ((9)-(11)). Undoubtedly, if MCMC converges, there will be a high density of MCMC samples near the posterior probability, i.e., regions with larger $\exp[\eta(\mathbf{x}_{\text{syn}})]$. By probing how $\exp[\eta(\mathbf{x}_{\text{syn}})]$ varies as N_b changes, we have a better understanding of the effect of the choice of N_b on the accuracy of the posterior distribution estimation. In particular, while decreasing N_b , we measure the difference introduced by using $\exp[\eta(\tilde{\mathbf{x}})]$ compared to $\exp[\eta(\mathbf{x}_{\text{syn}})]$, where $\tilde{\mathbf{x}}$ again denotes the interpolated path from N_b knots extracted from \mathbf{x}_{syn} . We first calculate the true value

$$\exp[\eta(\mathbf{x}_{\text{syn}})] \triangleq \exp\left[\frac{q}{\sigma^2}(\mathbf{D}_{\text{syn}}^H \mathbf{y})^H (\mathbf{D}_{\text{syn}}^H \mathbf{y})\right] \quad (42)$$

TABLE V
RUNTIME AS A FUNCTION OF NUMBER OF BLOCKS AND NUMBER OF ITERATIONS

N_b	Iterations			
	5×10^3	10^4	5×10^4	10^5
20	0.2771s	0.5717s	2.9692s	5.7394s
200	0.6078s	1.1936s	5.9269s	12.8379s
1000	2.4641s	4.9219s	25.4540s	51.1769s

using noisy synthetic data \mathbf{y} and $\mathbf{D}_{\text{syn}} \triangleq \exp(j2\pi\phi_{\text{syn}})$, where ϕ_{syn} stands for the synthetic phase path. This value provides an upper bound. Then we compute

$$\exp[\eta(\tilde{\mathbf{x}})] \triangleq \exp\left[\frac{q}{\sigma^2}(\tilde{\mathbf{D}}^H \mathbf{y})^H (\tilde{\mathbf{D}}^H \mathbf{y})\right], \quad (43)$$

where $\tilde{\mathbf{D}} = \exp(j2\pi\tilde{\phi})$. Here $\tilde{\phi}$ is related to ϕ_{syn} by

$$\tilde{\phi}(t_n) = \begin{cases} \phi_{\text{syn}}(t_n), & (n-1)/M \in \mathbb{Z}, \\ \text{Interp}\left(\phi_{\text{syn}}(t_{M\lfloor \frac{n-1}{M} \rfloor + 1}), \phi_{\text{syn}}(t_{M\lceil \frac{n-1}{M} \rceil + 1})\right), & \text{else} \end{cases} \quad (44)$$

for $n = 1, \dots, N$ with $M = N/N_b$. The coarse-grained absolute value of the error in calculating Bayesian evidence as a result of interpolation is reflected in $\epsilon = |\exp[\eta(\mathbf{x}_{\text{syn}})] - \exp[\eta(\tilde{\mathbf{x}})]|$. The error ϵ versus N_b is plotted in the lower panel of Fig. (2). Observe that for e.g., $N_b = 20$ (red circle), almost 90% of the information is retained in the reduced \mathbf{M}_2^b with $\epsilon < 10^{-3}$. We believe that computing the entropy in (41) provides us an alternative way to select N_b . However, further investigation is required to justify the claim. In the following sections, we show in simulations that the choices of, for example, $N_b = 20$, maintains MCMC performance in both estimation and detection, while saving computational resources significantly. This is reflected in Table (V), where MCMC runtime averages over 10^3 experiments for different N_b 's with different number of iterations are reported, specifically for $N_{\text{iteration}} = 5 \times 10^3, 10^4, 5 \times 10^4, 10^5$. The runtimes are computed on a 2.4GHz central processing unit (CPU).

E. Estimation performance

Throughout this and the next section, we fix $N_b = 5$ for the HMM (explained in Section VI-D1), and vary N_b for the MCMC.

1) MCMC-posterior for the state path: $\Pr(\mathbf{x}|\mathbf{y})$

In Fig. (3), a cross-section of the MCMC-posterior $\Pr(\mathbf{x}|\mathbf{y})$ at time instant t_5 for SNR = 0.15 and $N_b = 20$ is shown. The performance at other epochs is similar.

Trace plots and histograms for $f(t_5)$ and $\phi(t_5)$, respectively, are shown. By definition, trace plots show the sampled values of a parameter over time. They reflect whether and how fast MCMC converges in distribution. Starting from a random initial point, MCMC converges after about 10^3 iterations. This, so called ‘‘burn in’’ period is seen in the top and third panels in Fig. (3), compressed into the left edge of the plots. After the ‘‘burn in’’ period, the samples drawn from the MCMC have values centered around the true value, with bias less than 0.0005 Hz (0.05 percent of the bandwidth) and 0.02 rad, and standard deviation less than 0.002 Hz and 0.5 rad for $f(t_5)$ and

$\phi(t_5)$, respectively. This conclusion can also be drawn from the histograms on the second and fourth panels in Fig. (3), the shapes of which, by definition, resemble the true posterior distributions $\Pr(f(t_5)|\mathbf{y})$ and $\Pr(\phi(t_5)|\mathbf{y})$.

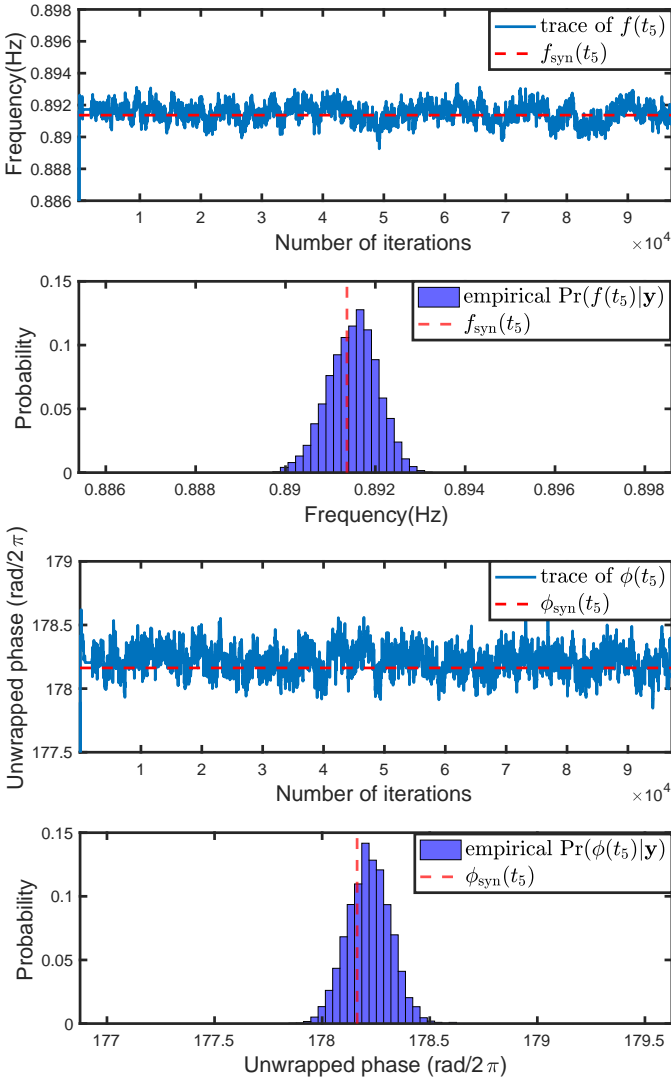


Fig. 3. MCMC convergence for $k = 1$ and $\text{SNR} = 0.15$. First panel: Trace plot of $f(t_5)$. Second panel: MCMC-posterior distribution $\Pr(f(t_5)|\mathbf{y})$. Third panel: Trace plot of $\phi(t_5)$. Fourth panel: MCMC-posterior distribution $\Pr(\phi(t_5)|\mathbf{y})$, where \mathbf{y} is generated from model $k = 1$. Injected parameters of synthetic data: $f_{\text{syn}}(t_5) = 0.8914\text{Hz}$, $\phi_{\text{syn}}(t_5) = 178.2324 \text{ rad}/2\pi$, $\text{SNR} = 0.15$.

2) MCMC-MAP estimator

A typical realization of the MCMC-MAP estimates of frequency paths $\mathbf{f}_{\text{MCMC}}^*$ for $N_b = 5, 20, 200$ and 1000 , compared with the HMM estimated frequency path is displayed in Fig. (4). Here we can see, that the dynamics of the wandering frequency is captured even by $N_b = 5$ knots.

In Fig. (5), we plot the root-mean-square-error (RMSE) of the MCMC-MAP estimated frequency path, normalized with respect to the path length N , defined to be $\text{RMSE} \triangleq \sqrt{E(\|\mathbf{f}_{\text{MCMC}}^* - \mathbf{f}_{\text{syn}}\|^2)/N}$, where $E(\cdot)$ denotes the sample mean over 10^3 experiments, and $\mathbf{f}_{\text{MCMC}}^*$ and \mathbf{f}_{syn} denote the MCMC-MAP estimated and synthetic frequency path, respec-

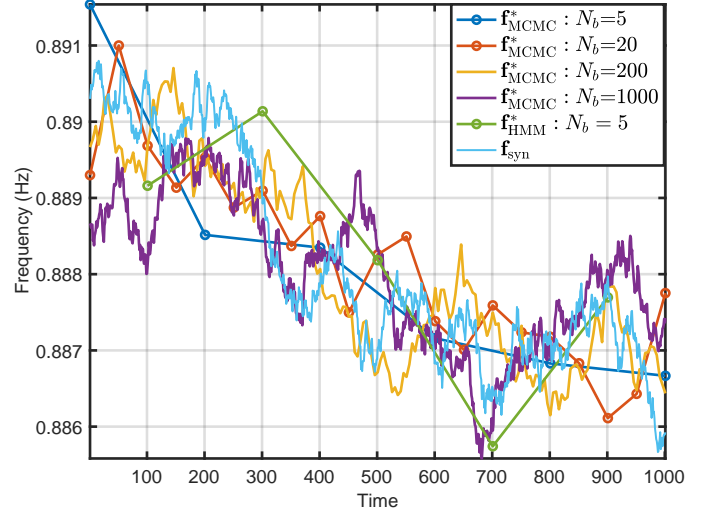


Fig. 4. MAP frequency estimate $\mathbf{f}_{\text{MCMC}}^*$ for $N_b = 5$ (blue), 20 (red), 200 (yellow) and 1000 (purple) of the MCMC and $N_b = 5$ (green) of the HMM at $\text{SNR} = 0.15$. The wandering dynamics of the frequency is captured even with $N_b = 5$ knots.

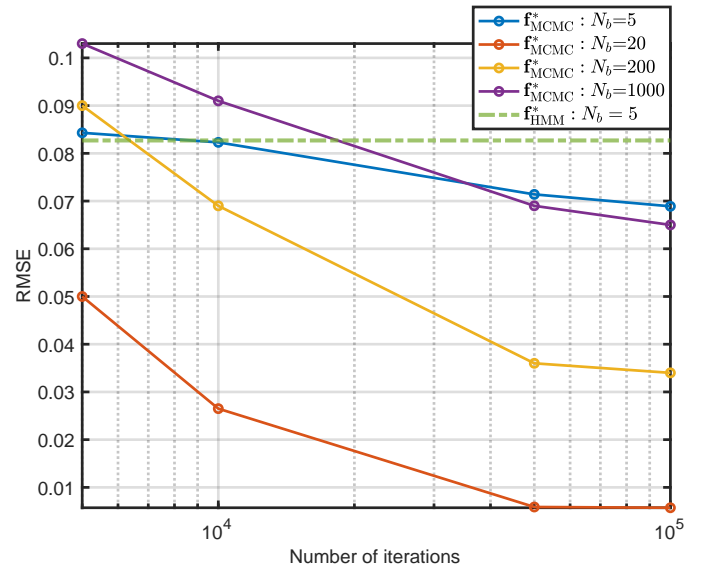


Fig. 5. RMSE of MCMC estimate as a function of number of blocks and number of iterations for $N_b = 5$ (blue), 20 (red), 200 (yellow) and 1000 (purple) and $N_b = 5$ (green) of HMM at $\text{SNR} = 0.15$. Among all, MCMC with $N_b = 20$ achieves the lowest mean error.

tively. In this example, every frequency point $f_{\text{MCMC}}^*(t_n)$ and $f_{\text{syn}}(t_n)$ takes values in the interval $[0, 1]$, giving the upper bound for RMSE of 1. As shown here, $N_b = 20$, among all, returns the lowest mean error and overall the MCMC-MAP estimator provides more accurate estimation against the HMM estimator, although at the cost of longer computing time.

F. Detection performance

1) MCMC-posterior distribution for detection: $\Pr(k|\mathbf{y})$

In Fig. (6), two examples of the MCMC-posterior distribution $\Pr(k|\mathbf{y})$ for an $\text{SNR} = 0.15$ are presented. The

upper panel shows a typical trace plot of the parameter k for when the data contain no signal, where the value of k jumps constantly between $k = 0$ and $k = 1$. The histogram of this k is shown in the second panel. The third panel shows typical samples when the signal is present; after around 3×10^3 iterations, k clearly approaches the value 1. The lower panel depicts the histogram of k for this case.

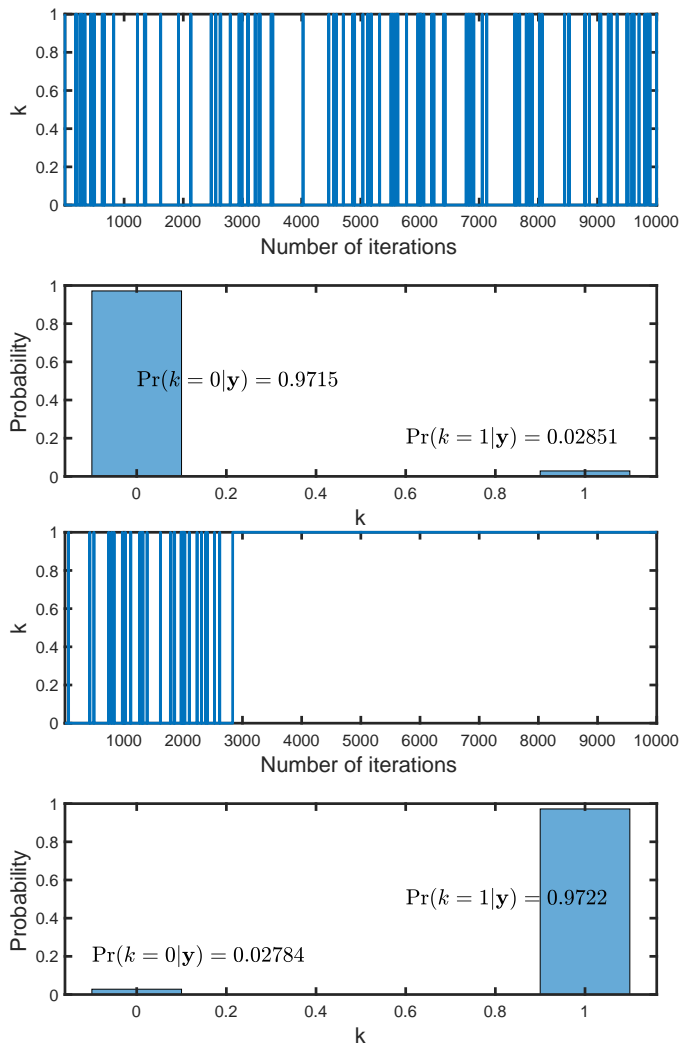


Fig. 6. Trace plot and histogram (posterior distribution) of k . Upper panel: Trace plot of k with synthetic data $k = 0$. Second panel: Posterior distribution $\Pr(k = 0|y)$ with synthetic data $k = 0$. Third panel: Trace plot of k with synthetic data $k = 1$ and $\text{SNR} = 0.15$. Lower panel: Posterior distribution $\Pr(k = 1|y)$ with synthetic data $k = 1$ and $\text{SNR} = 0.15$.

2) Receiver operating characteristic

Receiver operating characteristic (ROC) curves for an omniscient,³ The MCMC detector and the HMM detector are shown in Fig. (7), (8) and (9), computed over 10^5 simulation runs at $\text{SNR} = 0.15, 0.1$ and 0.2 respectively for synthetic signals with frequencies wandering according to (5) and (6), with $\gamma_{\text{syn}} = 10^{-4} \text{ Hz sec}^{-1/2}$.

³The omniscient detector is based on the assumption that the true path \mathbf{x}_{syn} is known. It provides an upper bound for the probability of detection.

The upper panels are for the MCMC algorithm with parameters $\gamma = 10^{-4} \text{ Hz sec}^{-1/2}$, and the lower panels are for $\gamma = 10^{-5} \text{ Hz sec}^{-1/2}$. The mismatch in γ and γ_{syn} appears to cause degradation in the MCMC detector performance. This sensitivity to γ is an unwanted effect and requires further investigation.

At relatively high $\text{SNR} = 0.2$, the plots show that the MCMC detector outperforms the HMM detector across the whole Pf range. For $\text{SNR} = 0.1$, the detection rate for the MCMC detector, although higher than the HMM detector, is quite low, i.e., around 0.17 at $\text{Pf} = 10^{-2}$. At $\text{SNR} = 0.15$ both the MCMC detector and the HMM detector demonstrate better performance than when the $\text{SNR} = 0.1$ with the MCMC outperforming the HMM. In particular, for a false alarm probability $\text{Pf} = 10^{-2}$, the detection probability Pd of the MCMC detector is around 0.8 with matched γ 's, while dropping below 0.7 with mismatched γ 's. In Fig. (7), when $\text{SNR} = 0.15$, the MCMC detector outperforms the HMM detector across the Pf range greater than 10^{-2} for all choices of N_b and γ . The HMM performs “detection after estimation”, i.e., it calculates the most likely frequency path first, then compares the statistics of this path with the statistics of the noise, while the detection is directly embedded in the design of the MCMC detector. As a result, the HMM's detection performance is heavily dependent on the accuracy of estimation, as opposed to the MCMC detector, where estimation becomes a consequence of detection. The degradation of performance at low SNR, known as the “threshold effect” is a common problem in nonlinear estimation. Even though we are not able to derive it mathematically, we infer from the plots that the threshold effect for MCMC detector happens between $\text{SNR} = 0.15$ and $\text{SNR} = 0.1$.

Fig. (7), (8) and (9) also show that N_b has little effect on the overall detection performance of the MCMC detector. The red, yellow and purple curves overlap each other, especially when $\text{Pf} < 10^{-1}$.

In Fig. (10), we fix the false alarm probability $\text{Pf} = 10^{-2}$ and plot Pd versus SNR varying from 0.1 to 0.25 for the MCMC detector with $N_b = 20$ and the HMM detector respectively. Controlling the false alarm probability to be no more than 10^{-2} is typically tolerated in gravitational wave astrophysics applications [24]. Similarly, the upper panel and lower panels show the MCMC detector's performance without and with mismatch in γ , respectively. In both plots the MCMC detector has higher detection probability than the HMM detector, even with γ mismatched. For example when the $\text{SNR} = 0.15$, the MCMC detector outperforms the HMM detector with 25% higher detection probability.

VII. CONCLUSION

In this work a Bayesian posterior density for detecting sinusoidal signals with wandering frequency in noise is derived and computed. The method is based on MCMC techniques. As part of the algorithm, our method provides computation of the posterior density of the signal parameters. For efficient computation of this density we propose a knot-interpolating technique, where we sample the signal parameters at the

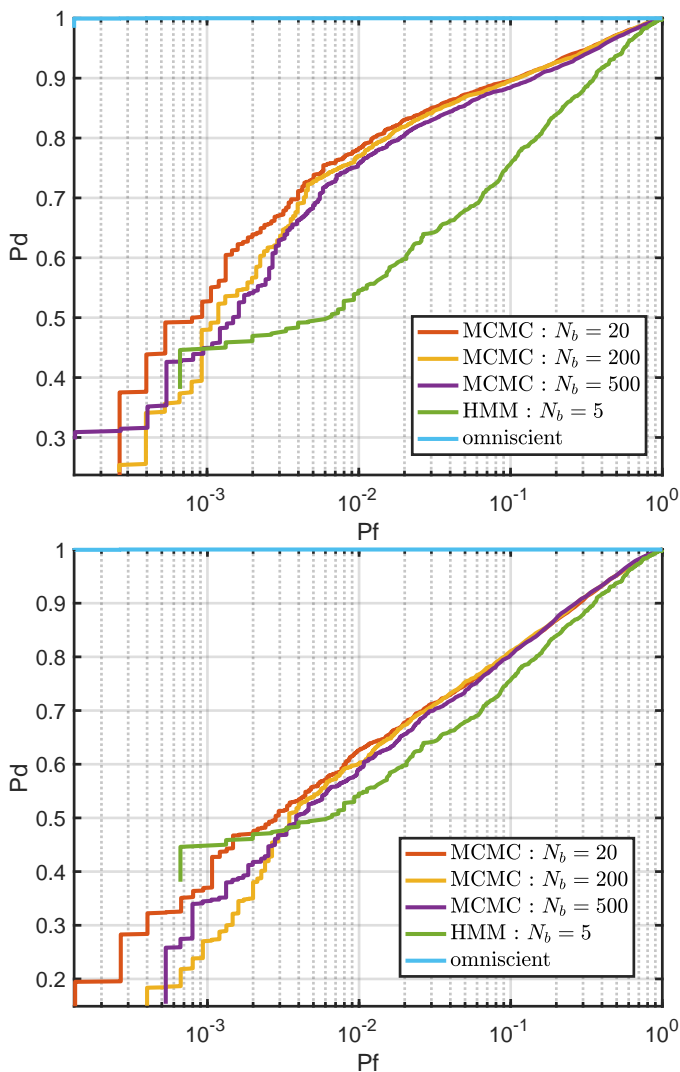


Fig. 7. ROC curves at SNR = 0.15 for MCMC with $N_b = 20$ (red), 200 (yellow), 500 (purple) and HMM with $N_b = 5$ (green). The upper panel shows ROC curves for $\gamma = 10^{-4} \text{ Hz sec}^{-1/2}$, and lower panel for $\gamma = 10^{-5} \text{ Hz sec}^{-1/2}$. The HMM detector yields worse performance when $\text{Pf} > 10^{-3}$. The omniscient detector (blue curve) provides an upper bound.

coarsely spaced time knots, while the rest of the signal is recovered by the interpolation between the knots. A procedure for selecting a reasonable number N_b of knots, given the signal dynamics is presented and justified. This procedure relies on the computation of the (von Neumann) entropy of the dynamics matrices. Although we cannot claim its optimality, we illustrate by experiments how the procedure provides a balance between the runtime and detection and estimation accuracy.

In addition, we have developed an algorithm within MCMC for proposing new state paths that are arbitrarily close to the previous path. This method ensures dense selection of MCMC samples for highly structured multi-dimensional vectors. The full description of the algorithm is provided.

The performance of the MCMC is evaluated in terms of mean estimation errors and ROC curves and compared with

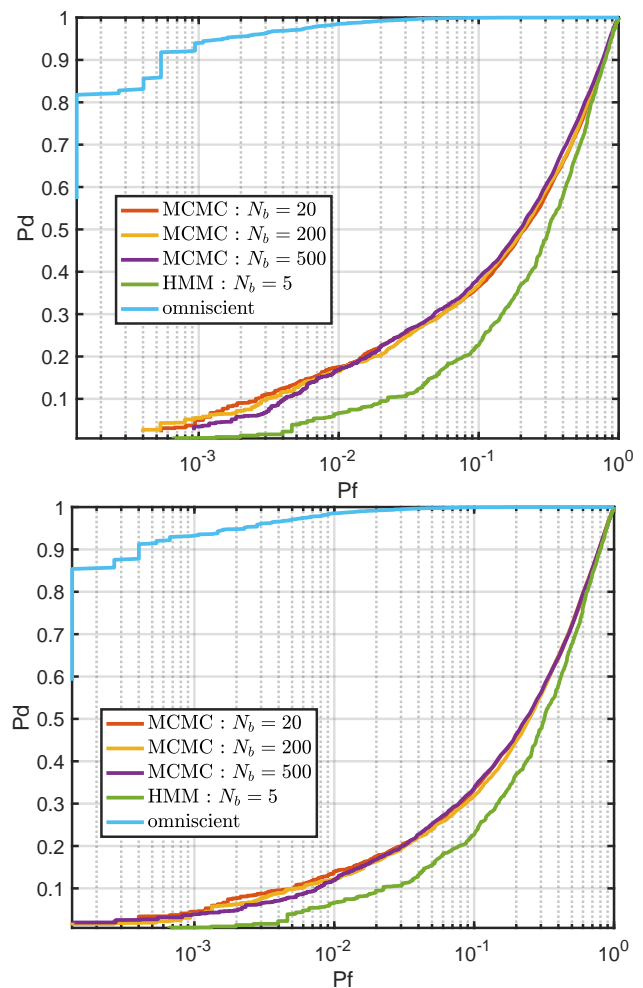


Fig. 8. ROC curves at SNR = 0.1 for MCMC with $N_b = 20$ (red), 200 (yellow), 500 (purple) and HMM with $N_b = 5$ (green). The upper panel shows ROC curves for $\gamma = 10^{-4} \text{ Hz sec}^{-1/2}$, and lower panel for $\gamma = 10^{-5} \text{ Hz sec}^{-1/2}$. The HMM detector yields the worst performance. The omniscient detector (blue) provides an upper bound.

the performance of the HMM-based Viterbi algorithm. We demonstrate that our algorithm presents both higher detection rates and greater estimation accuracy in all of the experiments conducted. In particular, the simulation results show that our method outperforms the HMM in estimation accuracy by around 5% and improves detection rate by up to 25%.

REFERENCES

- [1] P. Jaranowski, A. Królak, and B. F. Schutz, "Data analysis of gravitational-wave signals from spinning neutron stars: The signal and its detection," *Physical Review D*, vol. 58, Aug 1998.
- [2] K. Riles, "Gravitational waves: Sources, detectors and searches," *Progress in Particle and Nuclear Physics*, vol. 68, p. 1–54, Jan 2013.
- [3] A. Melatos and B. Link, "Pulsar timing noise from superfluid turbulence," *Monthly Notices of the Royal Astronomical Society*, vol. 437, pp. 21–31, 11 2013.
- [4] P. Jančovič and M. Kökür, "Detection of sinusoidal signals in noise by probabilistic modelling of the spectral magnitude shape and phase continuity," in *2011 IEEE International Conference on Acoustics, Speech and Signal Processing (ICASSP)*, pp. 517–520, IEEE, 2011.
- [5] B. Comar, "Detection of sinusoids with frequency drift in white gaussian noise," in *2021 9th International Conference on Information and Communication Technology (ICOICT)*, pp. 291–296, IEEE, 2021.

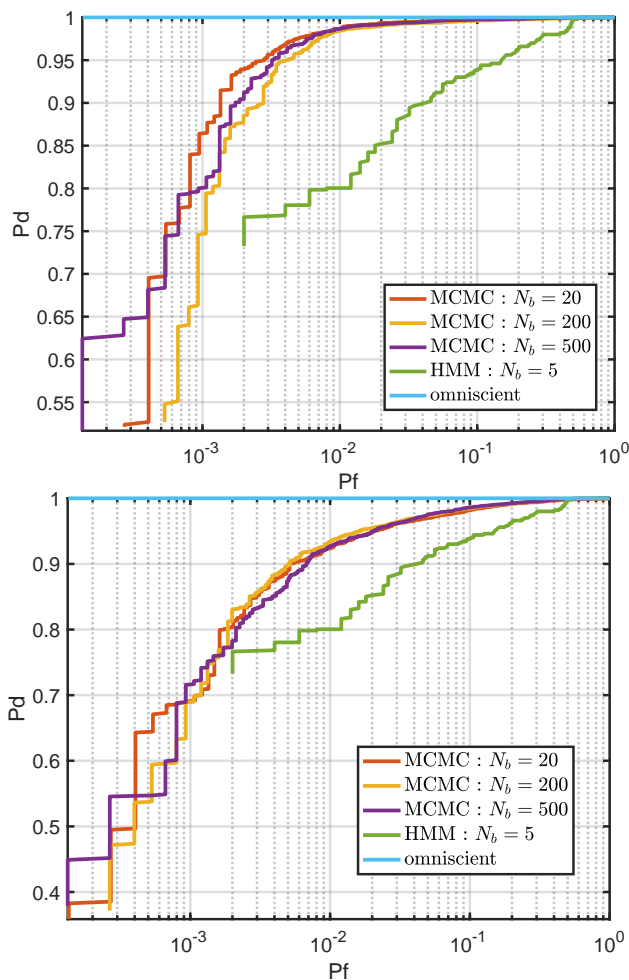


Fig. 9. ROC curves at SNR = 0.2 for MCMC with $N_b = 20$ (red), 200 (yellow), 500 (purple) and HMM with $N_b = 5$ (green). The upper panel shows ROC curves for $\gamma = 10^{-4} \text{ Hz sec}^{-1/2}$, and lower panel for $\gamma = 10^{-5} \text{ Hz sec}^{-1/2}$. Overall, the MCMC detector has overall better performance. The omniscient detector (blue) provides an upper bound.

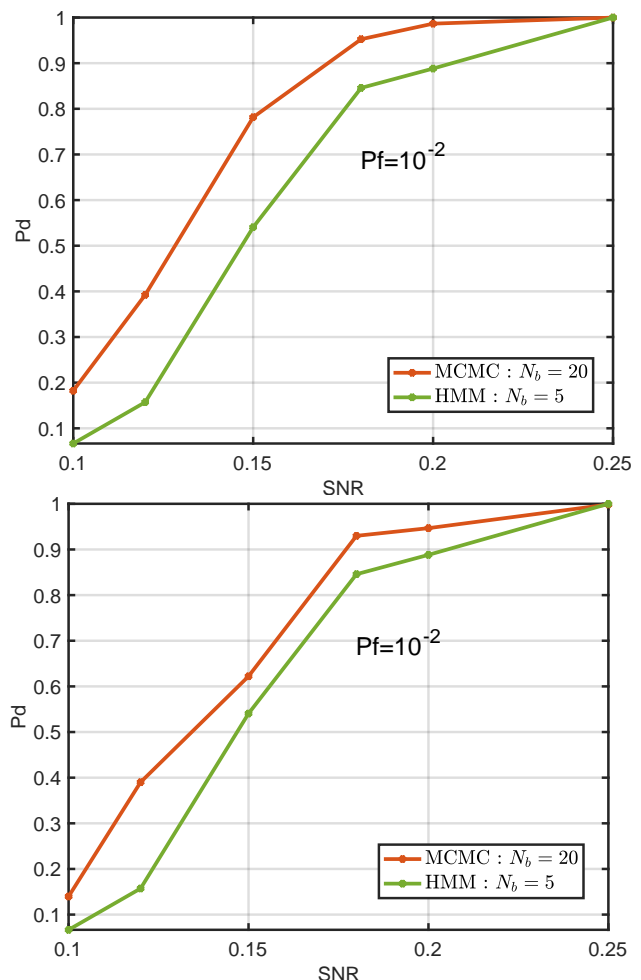


Fig. 10. Detection probability Pd versus SNR ranging from 0.1 to 0.25, with false alarm rate $P_f = 10^{-2}$ for MCMC with $N_b = 20$ (red) and HMM with $N_b = 5$ (green). The upper panel shows ROC curves for $\gamma = 10^{-4} \text{ Hz sec}^{-1/2}$, and lower panel for $\gamma = 10^{-5} \text{ Hz sec}^{-1/2}$. MCMC has higher detection probability than HMM across the SNR range regardless of the bias in γ .

[6] L. V. Tuan, M. Korotina, A. Bobtsov, S. Aranovskiy, and A. Pyrkina, "On-line estimation of time-varying frequency of a sinusoidal signal—this work was supported by ministry of education and science of the Russian Federation, grant 8.8885.2017/8.9.," *IFAC-PapersOnLine*, vol. 52, no. 29, pp. 245–250, 2019. 13th IFAC Workshop on Adaptive and Learning Control Systems ALCOS 2019.

[7] L. Xiaocong and M. Xuanren, "An instantaneous frequency identification algorithm for time-varying frequency signals," *IEEE Access*, vol. 7, pp. 165345–165355, 2019.

[8] H. V. Poor, *An introduction to signal detection and estimation*. Springer Science & Business Media, 2013.

[9] T. Kailath and H. V. Poor, "Detection of stochastic processes," *IEEE Transactions on Information Theory*, vol. 44, no. 6, pp. 2230–2231, 1998.

[10] C. Georghiades and D. Snyder, "A proposed receiver structure for optical communication systems that employ heterodyne detection and a semiconductor laser as a local oscillator," *IEEE Transactions on Communications*, vol. 33, no. 4, pp. 382–384, 1985.

[11] F. M. Gardner, *Phaselock techniques*. John Wiley & Sons, 2005.

[12] C. Baker, "Optimum quadratic detection of a random vector in gaussian noise," *IEEE Transactions on Communication Technology*, vol. 14, no. 6, pp. 802–805, 1966.

[13] O. Macchi and L. Scharf, "A dynamic programming algorithm for simultaneous phase estimation and data decoding on random-phase channels," *IEEE Transactions on Information Theory*, vol. 27, no. 5, pp. 581–595, 1981.

[14] R. Short and J. Toomey, "Detection and estimation of frequency-random signals (corresp.)," *IEEE Transactions on Information Theory*, vol. 28, no. 6, pp. 940–946, 1982.

[15] L. Scharf, D. Cox, and C. Masreliez, "Modulo-2 π phase sequence estimation (corresp.)," *IEEE Transactions on Information Theory*, vol. 26, no. 5, pp. 615–620, 1980.

[16] S. Suvorova, A. Melatos, R. J. Evans, W. Moran, P. Clearwater, and L. Sun, "Phase-continuous frequency line track-before-detect of a tone with slow frequency variation," *IEEE Transactions on Signal Processing*, vol. 66, no. 24, pp. 6434–6442, 2018.

[17] I. Djurović and L. Stanković, "An algorithm for the wigner distribution based instantaneous frequency estimation in a high noise environment," *Signal Processing*, vol. 84, no. 3, pp. 631–643, 2004.

[18] C. Andrieu, N. De Freitas, A. Doucet, and M. Jordan, "An introduction to MCMC for machine learning," *Machine Learning*, vol. 50, pp. 5–43, Jan. 2003.

[19] C. Andrieu and A. Doucet, "Joint bayesian model selection and estimation of noisy sinusoids via reversible jump MCMC," *IEEE Transactions on Signal Processing*, vol. 47, no. 10, pp. 2667–2676, 1999.

[20] P. J. Green, "Reversible jump markov chain monte carlo computation and bayesian model determination," *Biometrika*, vol. 82, no. 4, pp. 711–732, 1995.

[21] G. L. Jones and J. P. Hobert, "Honest exploration of intractable probability distributions via markov chain monte carlo," *Statistical Science*, pp. 312–334, 2001.

[22] V. V. Veeravalli and H. V. Poor, "Quadratic detection of signals with drifting phase," *The Journal of the Acoustical Society of America*, vol. 89, no. 2, pp. 811–819, 1991.

[23] D. E. Simmons, J. P. Coon, and A. Datta, "Symmetric laplacians,

quantum density matrices and their von-neumann entropy.” *Linear Algebra and its Applications*, vol. 532, pp. 534–549, 2017.

- [24] B. P. Abbott, R. Abbott, T. D. Abbott, S. Abraham, F. Acernese, K. Ackley, C. Adams, R. X. Adhikari, V. B. Adya, C. Affeldt, *et al.*, “Search for gravitational waves from Scorpius X-1 in the first Advanced LIGO observing run with a hidden Markov model,” *Phys. Rev. D*, vol. 95, p. 122003, June 2017.

APPENDIX A: PROOF OF (6)

We consider a more general process where continuous frequency and phase path are described by

$$df(t) = -\frac{1}{\tau}f(t)dt + \gamma dB(t) \quad (45a)$$

$$\phi(t) = \int_0^t f(s)ds \quad (45b)$$

where τ and γ are called the *relaxation time* and the *diffusion constant*.

The variance and covariance of the time sampled variable $f(t+T)$ and $\phi(t+T)$ at time $t+T$, with time increments $T > 0$ are derived in [16] to be

$$\sigma_1^2 \triangleq \text{var}\{f(t+T)\} = (\gamma^2\tau/2)(1 - e^{-2T/\tau}) \quad (46a)$$

$$\sigma_2^2 \triangleq \text{var}\{\phi(t+T)\} = \gamma^2\tau^3[T/\tau - 2(1 - e^{-Tt/\tau}) + \frac{1}{2}(1 - e^{-2Tt/\tau})] \quad (46b)$$

$$\mathbf{K} \triangleq \text{cov}\{f(t+T), \phi(t+T)\} = (\gamma^2\tau^2/2)(1 - 2e^{-T/\tau} + e^{-2T/\tau}) \quad (46c)$$

We consider $f(t)$ to be a Wiener process with diffusion constant γ and $\tau = \infty$. Equation (46) is then approximated by

$$\sigma_1^2 \approx \sigma^2T \quad (47a)$$

$$\sigma_2^2 \approx \sigma^2T^3/3 \quad (47b)$$

$$\mathbf{K} \approx \sigma^2T^2/2 \quad (47c)$$

and we obtain the covariance matrix (6).

APPENDIX B: PSEUDOCODE

Algorithm 1: function ”Interp”

Input: $(\mathbf{x}(t_{n_1}), \mathbf{x}(t_{n_2}))$.

Output: $\{\tilde{\mathbf{x}}(t_{n_1}), \tilde{\mathbf{x}}(t_{n_1+1}), \tilde{\mathbf{x}}(t_{n_1+2}), \dots, \tilde{\mathbf{x}}(t_{n_2})\}$.

1

$$\begin{cases} \tilde{\phi}(t_{n_1+\ell}) = \phi(t_{n_1}) + f(t_{n_1})T\ell + \frac{1}{2}b_1(T\ell)^2 + \frac{1}{3}b_2(T\ell)^3 \\ \tilde{f}(t_{n_1+\ell}) = f(t_{n_1}) + b_1T\ell + b_2(T\ell)^2, \end{cases} \quad (48)$$

with

$$\begin{bmatrix} b_1 \\ b_2 \end{bmatrix} = \begin{bmatrix} T_b^2/2 & T_b^3/3 \\ T_b & T_b^2 \end{bmatrix}^{-1} \begin{bmatrix} \phi(t_{n_2}) - \phi(t_{n_1}) - f(t_{n_1})T_b \\ f(t_{n_2}) - f(t_{n_1}) \end{bmatrix} \quad (49)$$

for $\ell = 0, 1, \dots, n_2 - n_1$ with $T_b = t_{n_2} - t_{n_1}$.

⁴In our MCMC algorithms, we do not sample \tilde{a} to evaluate (22), but only compute the MAP estimate of \tilde{a} for a realization of \mathbf{D}_f , which is \bar{a} and we simply set the amplitude proposals $\tilde{a}' = \bar{a}$.

Algorithm 2: MCMC algorithm for joint detection estimation

1 Initialization: $k^1 \sim \text{Bernoulli}(1 - \alpha)$, $\tilde{\mathbf{x}}(t_1) = [\tilde{f}(t_1), \tilde{\phi}(t_1)]$, $\Pr(s^1) = [\alpha \ 1 - \alpha]^T$;
2 Sample $u_1 \sim \mathcal{U}(0, 1)$, $u_2 \sim \mathcal{U}(0, 1)$;
3 **if** $u_1 < \alpha$ **then**
4 | $k^1 = 0$, $\tilde{f}(t_1) = \emptyset$, $\tilde{\phi}(t_1) = \emptyset$, where the symbol
| \emptyset indicates that $\tilde{\mathbf{x}}^i$ is meaningless for $k = 0$
5 **else**
6 | $k^1 = 1$, $\tilde{f}(t_1) \sim \mathcal{U}(0, U)$, $\tilde{\phi}(t_1) = 0$
7 **end**
8 **begin**
9 | **for** $i = 2 : N_{\text{iteration}}$ **do**
10 | | Update $\Pr(s^i = 0) = \Gamma_{00} \Pr(s^{i-1} = 0) + \Gamma_{10} \Pr(s^{i-1} = 1)$;
11 | | **if** $\Pr(s^i = 0) > u_2$ **then**
12 | | | $s^i = 1$;
13 | | | **else**
14 | | | $s^i = 0$;
15 | | | **end**
16 | | Evaluate s^i and k^{i-1} ;
17 | | **if** $k^{i-1} = 0$ **and** $s^i = 1$ **then**
18 | | | birth move: go to Algorithm 4;
19 | | **else if** $k^{i-1} = 1$ **and** $s^i = 0$ **then**
20 | | | death move: go to Algorithm 5;
21 | | **else if** $k^{i-1} = 1$ **and** $s^i = 1$ **then**
22 | | | update: go to Algorithm 6;
23 | | **else**
24 | | | assign $(\tilde{\mathbf{x}}^i, \tilde{a}^i, k^i) = (\emptyset, \emptyset, 0)$.
25 | | **end**
26 | **end**
27 **end**

Algorithm 3: ”Birth” move

Input: $\tilde{\mathbf{x}}^{i-1}, \tilde{a}^{i-1}, k^{i-1}$.

Output: $\tilde{\mathbf{x}}^i, \tilde{a}^i, k^i$.

1 Propose a candidate state path according to Algorithm 6 (discussed in Section V-D);
2 Evaluate q (Equation (13a)) and \tilde{a}' based on $\tilde{\mathbf{x}}'$ obtained from Step 1 (Equation (13b));
3 Sample \tilde{a}' from distribution $\tilde{a}' \sim \mathcal{CN}(0, \sigma^2q)$; or (optional) let $\tilde{a}' = \bar{a}$ for simplicity if \bar{a} is of little interest to us⁴;
4 Evaluate W'_a and W'_f based on \tilde{a}' and $\tilde{\mathbf{x}}'$ (Equation (11)-(12));
5 Accept $(\tilde{\mathbf{x}}^i, \tilde{a}^i, k^i) = (\tilde{\mathbf{x}}', \tilde{a}', 1)$ with probability A_{birth} (Equation (30a)); otherwise set $(\tilde{\mathbf{x}}^i, \tilde{a}^i, k^i) = (\tilde{\mathbf{x}}^{i-1}, \tilde{a}^{i-1}, k^{i-1})$.

Algorithm 4: “Death Move”

Input: $\tilde{\mathbf{x}}^{i-1}, \tilde{a}^{i-1}, k^{i-1}$.

Output: $\tilde{\mathbf{x}}^i, \tilde{a}^i, k^i$.

- 1 Given previous value $\tilde{\mathbf{x}}^{i-1}$ and \tilde{a}^{i-1} (k^{i-1} must be 1);
 - 2 Evaluate W_a^{i-1} and W_f^{i-1} based on $\tilde{\mathbf{x}}^{i-1}$; \tilde{a}^{i-1}
(Equation (11)-(12));
 - 3 Accept $(\tilde{\mathbf{x}}^i, \tilde{a}^i, k^i) = (\emptyset, \emptyset, 0)$ with probability A_{death}
(Equation (30b)); otherwise set
 $(\tilde{\mathbf{x}}^i, \tilde{a}^i, k^i) = (\tilde{\mathbf{x}}^{i-1}, \tilde{a}^{i-1}, k^{i-1})$.
-

Algorithm 5: “update” move

Input: $\tilde{\mathbf{x}}^{i-1}, \tilde{a}^{i-1}, k^{i-1}$.

Output: $\tilde{\mathbf{x}}^i, \tilde{a}^i, k^i$.

- 1 Propose a candidate state path according to
Algorithm 7 (described in Section V-E);
 - 2 Evaluate q (Equation (13a)) and \tilde{a}' based on $\tilde{\mathbf{x}}'$
obtained from Step 1 (Equation (13b));
 - 3 Sample \tilde{a}' from distribution $\tilde{a}' \sim \mathcal{CN}(0, \sigma^2 q)$; or
(optional) let $\tilde{a}' = \tilde{a}$ for simplicity if \tilde{a} is of little
interest to us;
 - 4 Evaluate W_a' and W_f' based on \tilde{a}' and $\tilde{\mathbf{x}}'$
(Equation (11)-(12));
 - 5 Accept $(\tilde{\mathbf{x}}^i, \tilde{a}^i, k^i) = (\tilde{\mathbf{x}}', \tilde{a}', 1)$ with probability A_{update}
(Equation (30c)); otherwise set
 $(\tilde{\mathbf{x}}^i, \tilde{a}^i, k^i) = (\tilde{\mathbf{x}}^{i-1}, \tilde{a}^{i-1}, k^{i-1})$.
-

Algorithm 6: Generate a new proposal path \mathbf{x}' for the “birth” step

Input: \emptyset .

Output: $\tilde{\mathbf{x}}'$.

- 1 Initialization: $\tilde{\mathbf{x}}'(t_1) = \{\tilde{\phi}'(t_1), \tilde{f}'(t_1)\}$ with
 $\tilde{\phi}'(t_1) = 0, \tilde{f}'(t_1) \sim \mathcal{U}(0, U)$;
 - 2 Place the knots, i.e. determine the value for N_b and
the corresponding T_b, M ;
 - 3 Generate knot positioned path \mathbf{x}'_{N_b} , i.e. start from
 $\mathbf{x}'_{N_b}(1) = \tilde{\mathbf{x}}'(t_1)$ in Step 1, and follow the sampled
path model (Equation (32)), with random noise
 $\mathbf{w}(j) \stackrel{i.i.d.}{\sim} \mathcal{N}(\mathbf{0}, \mathbf{C})$ with \mathbf{C} given in Equation (33);
 - 4 Call function $\text{Interp}(\mathbf{x}'_{N_b}(j), \mathbf{x}'_{N_b}(j+1))$ for
 $j = 1, \dots, N_b - 1$ from Algorithm 1 and obtain the
proposed sample path $\tilde{\mathbf{x}}'$.
-

Algorithm 7: Generate a proposal path \mathbf{x}' for the “update” step

Input: $\tilde{\mathbf{x}}^{i-1}$

Output: $\tilde{\mathbf{x}}'$.

- 1 Extract N_b knots along $\tilde{\mathbf{x}}^{i-1}$ and form
 $\mathbf{x}_{N_b}^{i-1}(m+1) = \tilde{\mathbf{x}}^{i-1}(t_{mM+1})$ for $m = 0, \dots, N_b - 1$;
 - 2 Uniformly sample an integer $l \in \{1, 2, \dots, N_b\}$, and
determine the starting point $\mathbf{x}_{N_b}^{i-1}(l)$ to be the l th
element of $\mathbf{x}_{N_b}^{i-1}$; choose a value for β ;
 - 3 Determine the matrix \mathbf{M}'_1 and \mathbf{M}'_2 based on l from
Step 1 (Equation (36));
 - 4 Get previous noise sequence \mathbf{q}^{i-1} , which satisfies
 $\mathbf{M}'_2 \mathbf{q}^{i-1} = \mathbf{x}_{N_b}^{i-1} - \mathbf{M}'_1 \mathbf{x}_{N_b}^{i-1}(l)$;
 - 5 Generate a noise sequence
 $\mathbf{q}' = [\mathbf{q}^T(0), \dots, \mathbf{q}^T(N_b - 1)]^T$, where
 $\mathbf{q}_m^T \stackrel{i.i.d.}{\sim} \mathcal{N}(\mathbf{0}, \mathbf{I}_2)$;
 - 6 Compute new noise sequence \mathbf{q}^i via
 $\mathbf{q}^i = \mathbf{q}^{i-1} \cos \beta + \mathbf{q}' \sin \beta$; Generate proposed sample
path \mathbf{x}'_{N_b} , where $\mathbf{x}'_{N_b} = \mathbf{M}'_1 \mathbf{x}_{N_b}^{i-1}(l) + \mathbf{M}'_2 \mathbf{q}^i$;
 - 7 Call function $\text{Interp}(\mathbf{x}'_{N_b}(j), \mathbf{x}'_{N_b}(j+1))$ for
 $j = 1, \dots, N_b - 1$ from Algorithm 1 and obtain the
proposed sample path $\tilde{\mathbf{x}}'$.
-